

# Ultra-broadband soliton microcombs in resonantly-coupled microresonators

Kaixuan Zhu<sup>1\*</sup>, Xinrui Luo<sup>1\*</sup>, Yuanlei Wang<sup>1,2\*</sup>, Ze Wang<sup>1\*</sup>, Tianyu Xu<sup>1</sup>, Du Qian<sup>1</sup>, Yinke Cheng<sup>1,2</sup>, Junqi Wang<sup>1</sup>, Haoyang Luo<sup>1</sup>, Yanwu Liu<sup>1</sup>, Xing Jin<sup>1</sup>, Xin Zhou<sup>2</sup>, Min Wang<sup>2</sup>, Jian-Fei Liu<sup>2</sup>, Xuening Cao<sup>2</sup>, Ting Wang<sup>2</sup>, Qihuang Gong<sup>1,3,4</sup>, Bei-Bei Li<sup>2</sup>, and Qi-Fan Yang<sup>1,3,4†</sup>

<sup>1</sup>State Key Laboratory for Artificial Microstructure and Mesoscopic Physics and Frontiers Science Center for Nano-optoelectronics, School of Physics, Peking University, Beijing 100871, China

<sup>2</sup>Beijing National Laboratory for Condensed Matter Physics, Institute of Physics, Chinese Academy of Sciences, Beijing 100190, China

<sup>3</sup>Peking University Yangtze Delta Institute of Optoelectronics, Nantong, Jiangsu 226010, China

<sup>4</sup>Collaborative Innovation Center of Extreme Optics, Shanxi University, Taiyuan 030006, China

\*These authors contributed equally to this work.

†Corresponding author: leonardoyoung@pku.edu.cn

Soliton microcombs – equidistant spectral lines generated from nonlinear microresonators – have endowed integrated photonics with unprecedented precision and parallelization. However, generating broadband microcombs is challenged by the required pump power that scales quadratically with the number of comb lines. Here, we demonstrate that incorporating a resonant coupler passively enhances the effective pump power by several orders of magnitude, thereby expanding the soliton microcomb’s usable bandwidth by a factor of 3. Moreover, the resonant coupler enables unconventional tuning dynamics that facilitate thermally robust access to soliton states. Powered by an on-chip laser, the soliton microcomb delivers unprecedented spectral coverage. Our strategy overcomes the power constraints in generating broadband soliton microcombs and paves the way for their deployment in timing, metrology, and communications.

Optical frequency combs – spectra composed of equidistant, phase-coherent lines – are now realizable on photonic chips as soliton microcombs<sup>1</sup>. Generated in high-Q microresonators driven by continuous-wave light, these devices exploit a balance between Kerr nonlinearity and dispersion to produce stable, ultrashort circulating pulses<sup>2–4</sup>. Their compact architecture is indispensable for integrated applications, serving as precise frequency rulers in optical frequency synthesizers<sup>5</sup>, optical clocks<sup>6</sup>, and spectrometers<sup>7–9</sup> operable in challenging environments. Moreover, the inherently large comb spacings – often exceeding tens of gigahertz – render soliton microcombs ideally suited for multi-wavelength sources in wavelength-division multiplexing applications<sup>10–12</sup>.

Nevertheless, the transformative potential of optical frequency comb technology scales with the number of comb lines with sufficient power<sup>13–15</sup>. Although broadband soliton microcombs can be realized at high repetition rates (e.g., in the THz regime)<sup>16–18</sup>, they are typically too sparse for many practical applications. Denser combs are required to directly link the optical and microwave domains for complete comb stabilization<sup>19</sup> – and they also offer more channels for parallel information processing. However, achieving broadband soliton microcombs with dense line spacings is highly power-intensive, as the required pump power scales quadratically with the number of comb lines<sup>2,3,20,21</sup>. Recent strategies to circumvent this inefficient scaling include innovative pumping schemes, such as coupled-resonator architectures<sup>22,23</sup> and pulsed pump lasers<sup>24–26</sup>. In particular, the resonant coupler (RC) concept – previously demonstrated in fiber<sup>22</sup> and electro-optic resonators<sup>27</sup> – has been shown to broaden comb spectra markedly. Here, we extend RCs to

soliton microcombs, effectively boosting the pump power and yielding combs with spectral spans up to 3 times broader than conventional architectures.

## Results

### Principle

Soliton microcombs are conventionally generated in a nonlinear microresonator (NR) evanescently coupled to a bus waveguide. When the continuous-wave pump power  $P_{\text{in}}$  exceeds the parametric oscillation threshold  $P_{\text{th}}$ , four-wave mixing initiates sideband formation. For soliton formation, however, a higher pump power is required together with red detuning the pump relative to the cavity resonance. The span of soliton microcombs increases with the amount of red detuning, which is ultimately limited by the pump power. Specifically, to sustain a soliton microcomb spanning  $N$  lines within the 3 dB bandwidth, the pump power must satisfy

$$P_{\text{in}} \geq \frac{2D_2 P_{\text{th}} N^2}{\kappa_{\text{NR}}}, \quad (1)$$

where  $D_2$  and  $\kappa_{\text{NR}}$  are the group-velocity dispersion and the dissipation rate of the NR. Equation (1) reveals the quadratic scaling of pump power with comb bandwidth. Therefore, the required pump power to obtain a broadband comb can often exceed the output of typical laser diodes.

To overcome this limitation, we interpose an additional microresonator (RC) between the bus waveguide and the NR (Fig. 1A). In this configuration, the RC provides a resonant enhancement of the pump power; the enhanced pump power is delivered to the pump resonance of the

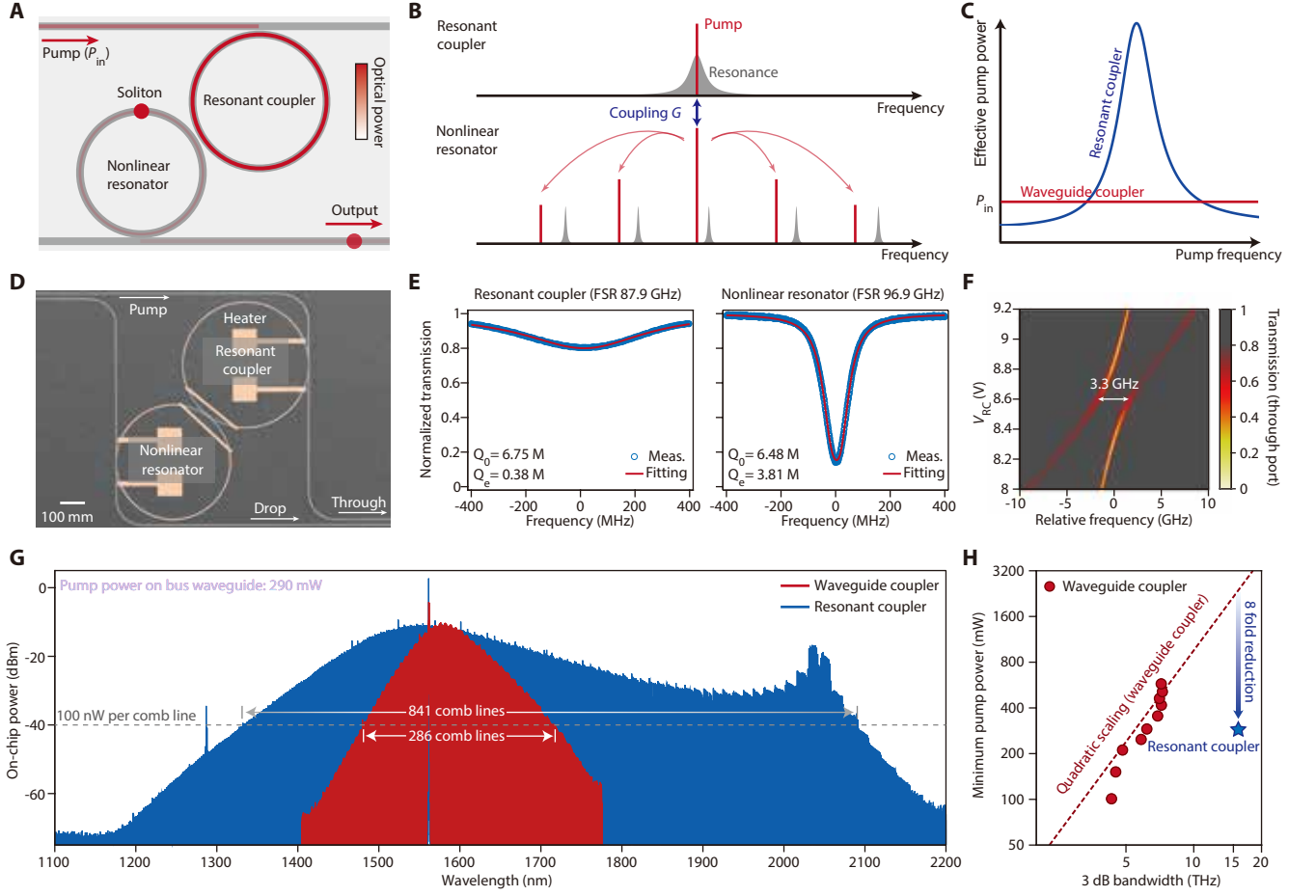


**Fig. 1. Concept and realization of resonantly-coupled microresonators.** (A) Schematic representation of a nonlinear microresonator pumped via a resonant coupler, with the optical power indicated by color. (B) Diagram illustrating the energy flow within the coupled system. (C) Effective pump power as a function of pump frequency. (D) Microscopic image of the fabricated coupled  $\text{Si}_3\text{N}_4$  microresonators. (E) Measured transmission spectra revealing the intrinsic quality factor  $Q_o$  and the external coupling quality factor  $Q_e$  for both the resonant coupler and the nonlinear microresonator. (F) Transmission spectra from the through port as a function of the voltage  $V_{RC}$  applied to the resonant coupler's heater. The minimum frequency difference between the hybridized modes is 3.3 GHz. (G) Comparison of optical spectra for soliton microcombs generated using conventional waveguide couplers (red) and resonant couplers (blue). All power refers to on-chip power. (H) Measured minimum pump power as a function of 3 dB bandwidth of soliton microcombs pumped via the waveguide coupler (red dots) and the resonant coupler (blue star). The red dashed line represents the quadratic scaling. The figure is plotted on a log-log scale.

NR via the inter-resonator coupling (Fig. 1B). Using a simplified model, the effective pump power delivered to the NR is enhanced by a factor on the order of

$$\Gamma = \frac{4G^2}{\kappa_{RC} \kappa_{NR}}, \quad (2)$$

where  $G$  is the coupling rate between the resonators and  $\kappa_{RC}$  is the RC's dissipation rate. The enhancement can reach tens to hundreds fold for  $G \gg \kappa_{NR}, \kappa_{RC}$ , enabling soliton microcombs with significantly broader spans. Unlike the waveguide coupler, the enhancement provided by the RC is frequency-dependent, with an effective bandwidth of approximately  $2\kappa_{RC}$  (Fig. 1C). A detailed anal-

ysis is provided in the Supplementary Materials.

### Device

We implement the proposed configuration using coupled  $\text{Si}_3\text{N}_4$  microresonators fabricated via subtractive processes<sup>28</sup> (Fig. 1D). The  $\text{Si}_3\text{N}_4$  core is 786 nm thick, with the RC and NR widths set to 1.5  $\mu\text{m}$  and 1.8  $\mu\text{m}$ , respectively. The minimum gap between the two microresonators is set to 200 nm. The free-spectral-range (FSR) of the RC and NR are 87.9 GHz and 96.9 GHz, respectively. The pump is coupled into the RC, and the resulting soliton microcomb is collected from the NR's drop port. Both resonators exhibit intrinsic quality factors of approximately 6–7 million, with external coupling

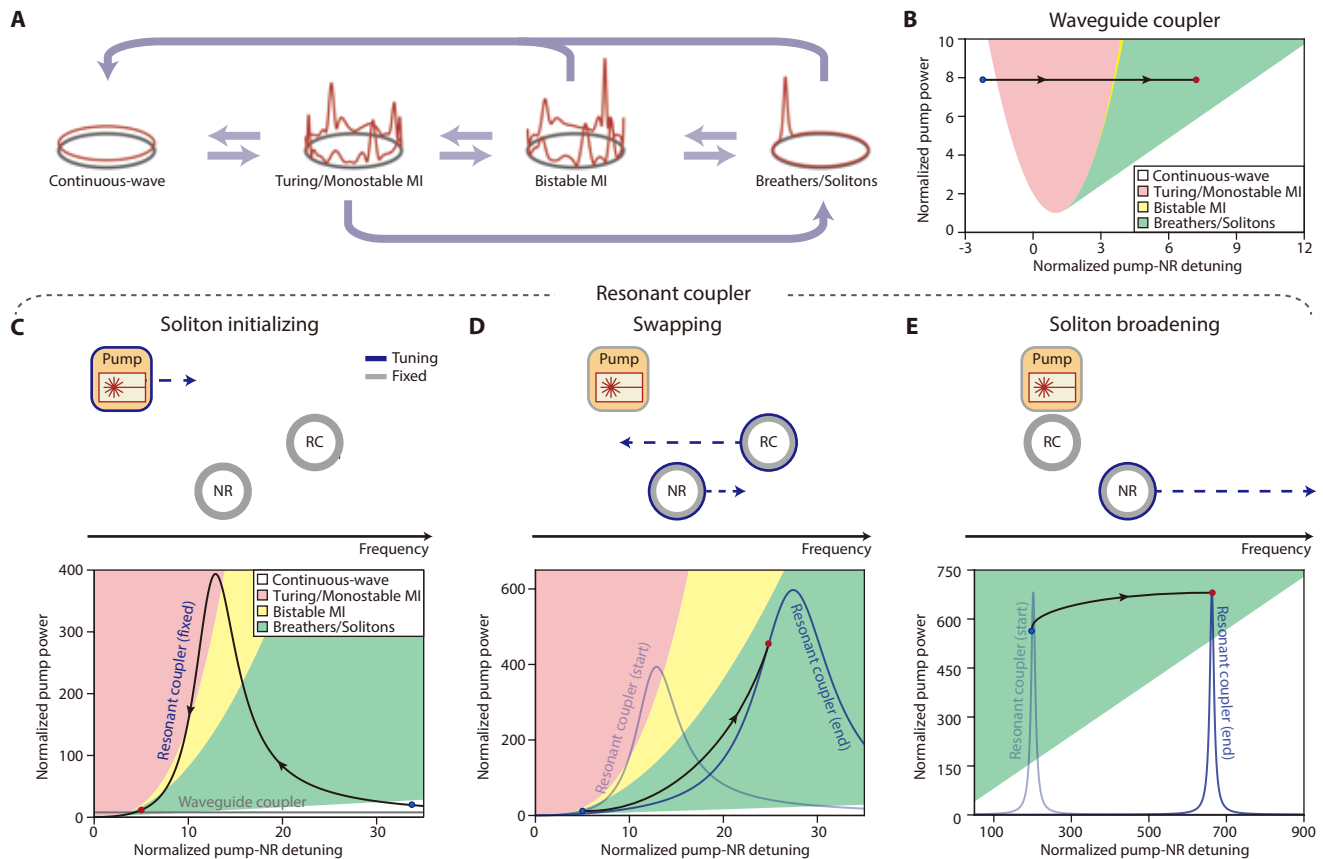


**Fig. 2. Pathway to soliton formation in phase diagrams.** (A) Schematic of the permissible transitions among distinct optical states in a nonlinear resonator (NR). (B) Phase diagram for a waveguide-coupled NR, where the black trajectory delineates the evolution to soliton states at constant pump power. Blue and red dots mark the initiation and termination of the tuning process, respectively. (C–E) Sequential stages for generating ultra-broadband solitons in a resonantly-coupled NR. The upper panels depict the relative frequency positions and tuning directions of the pump, resonant coupler (RC), and NR, while the lower panels illustrate their corresponding trajectories in the NR phase diagram. The blue curve represents the effective pump power delivered through the RC.

rates of 0.38 million (RC) and 3.81 million (NR) (see Fig. 1E). This design not only suppresses unwanted parametric oscillations in the RC but also broadens its resonance linewidth, affording a wider enhancement bandwidth for the pump. Integrated heaters facilitate independent tuning of the RC and NR resonances. By adjusting these heaters, we observe hybridized resonance shifts and avoided mode crossings, from which we infer a coupling rate of  $G = 2\pi \times 1.65$  GHz (Fig. 1F). The maximum enhancement factor, derived from these parameters, is on the order of a hundred (see Supplementary Materials).

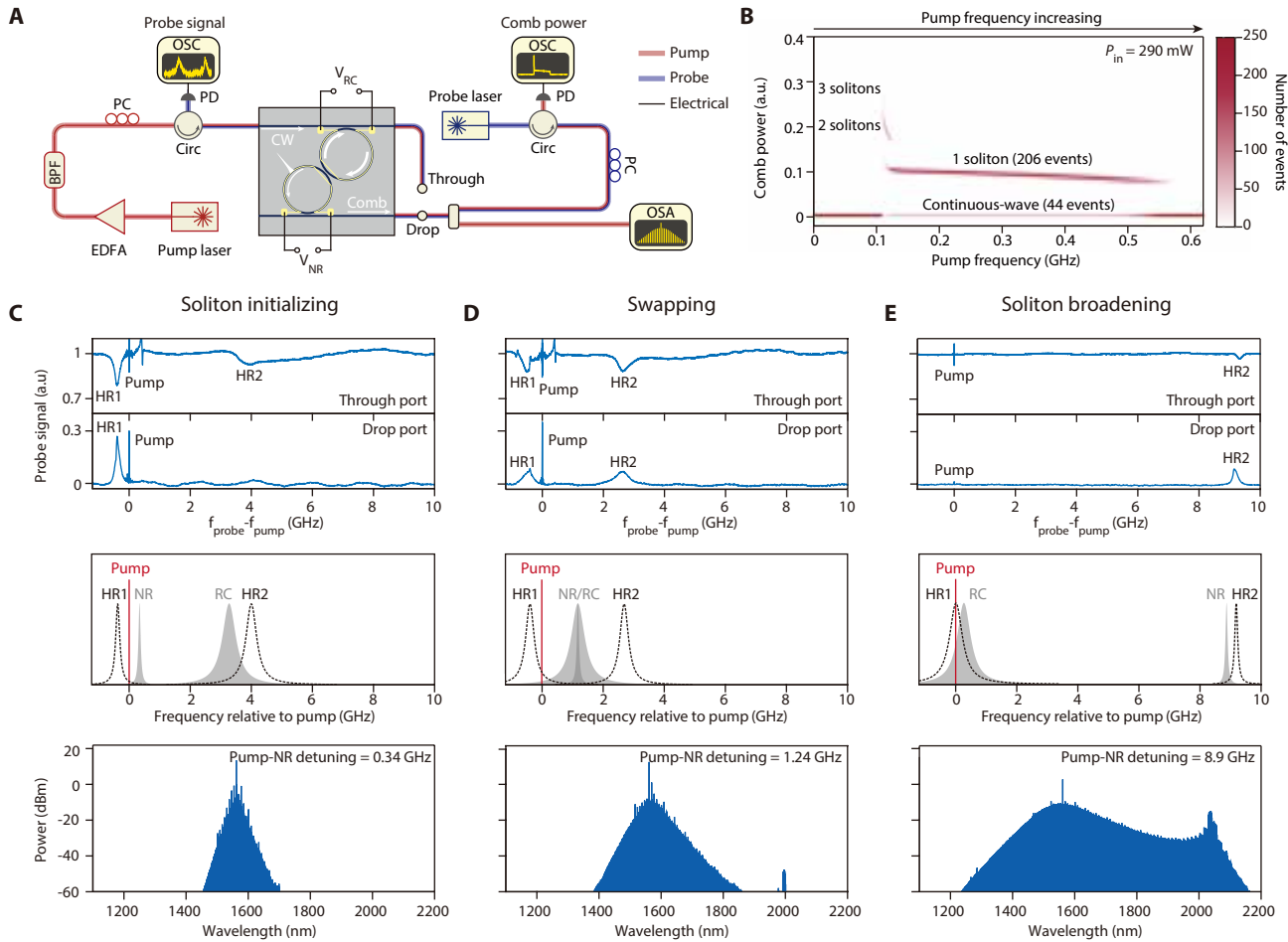
### Comb performance

Figure 1G compares soliton microcomb generation in NRs employing conventional waveguide couplers with that achieved via the RC approach. For an equitable comparison, the NR geometries and dissipation rates are maintained similar (see Supplementary Materials). Two key metrics are evaluated: the 3 dB bandwidth and the number of comb lines exceeding 100 nW. Under a 290 mW pump at 1561 nm, the waveguide-coupled NR pro-

duces its broadest soliton spectrum with a 3 dB bandwidth of 6.2 THz and 286 comb lines above 100 nW. In contrast, the RC configuration yields a significantly broadened spectrum, spanning 1160 to 2200 nm and exhibiting dispersive waves near 2050 nm due to higher-order dispersion effects<sup>4</sup> (see Supplementary Materials). This configuration achieves a 3 dB bandwidth of 15.8 THz and generates 841 comb lines above 100 nW, with comb line power near the spectral envelope center around -10.9 dBm. Furthermore, we measured the pump power required for the waveguide-coupled devices to deliver spectra comparable to those of the RC devices (Fig. 1H). Owing to the quadratic scaling of pump power with comb span, the waveguide-coupled devices are limited to a soliton span of only 7.2 THz, even when up to 600 mW is launched into the bus waveguide, which is substantially lower than the performance achieved using the RC architecture.

### Tuning dynamics

We then present the protocols to generate ultra-



**Fig. 3. Experimental access to ultra-broadband soliton microcombs.** (A) Experimental setup. EDFA: erbium-doped fiber amplifier; BPF: band-pass filter; PC: polarization controller; Circ: circulator; PD: photodetector; OSC: oscilloscope; OSA: optical spectrum analyzer. (B) Comb power versus pump laser frequency for 250 consecutive scans. The number of events is indicated by color. (C-E) Sequential stages for generating ultra-broadband solitons. Upper panels: recorded probe signals when the probe laser is launched from the through and drop ports. The hybridized resonances (HRs) and the beatnote with the backreflected pump are indicated. Middle panels: reconstructed frequencies of NR and RC relative to the pump. Lower panels: corresponding optical spectra of the soliton microcombs.

broadband soliton microcombs. The NR supports multiple optical states, yet direct access to the soliton state from the continuous-wave regime is unattainable<sup>2</sup> (Fig. 2A). Instead, soliton formation is initiated via modulational instability (MI), which in waveguide-coupled NRs is reached by precisely tuning the pump from the blue-detuned to the red-detuned side of the resonance (Fig. 2B). This MI-to-soliton transition typically involves a sharp intracavity power drop and a concomitant thermo-optic blue-shift that can destabilize the soliton state; various techniques, including rapid power modulation, have been developed to address this issue<sup>3,4</sup>.

In resonantly-coupled NRs, the tuning mechanism is fundamentally altered. Soliton initiation begins by setting the RC frequency to be blue-detuned relative to the NR (Fig. 2C), while the pump, initially red-detuned from

the NR, is tuned closer until MI is triggered. The tuning process is conveniently visualized using a phase diagram defined by the relative detuning between the pump and the NR and the effective pump power delivered to the NR. In this diagram, the effective pump curve, determined by the fixed frequencies of the RC and NR during the initial tuning stage, initially leads to an increase in intracavity power as the pump is tuned closer to the NR resonance. This increased power triggers modulational instability. As tuning continues, the effective pump power decreases, enforcing the transition into the soliton state. This tuning trajectory is effectively “backward” relative to the conventional approach.

To extend the comb span, the detuning is subsequently increased. Maintaining soliton operation under these conditions requires a corresponding increase in effective

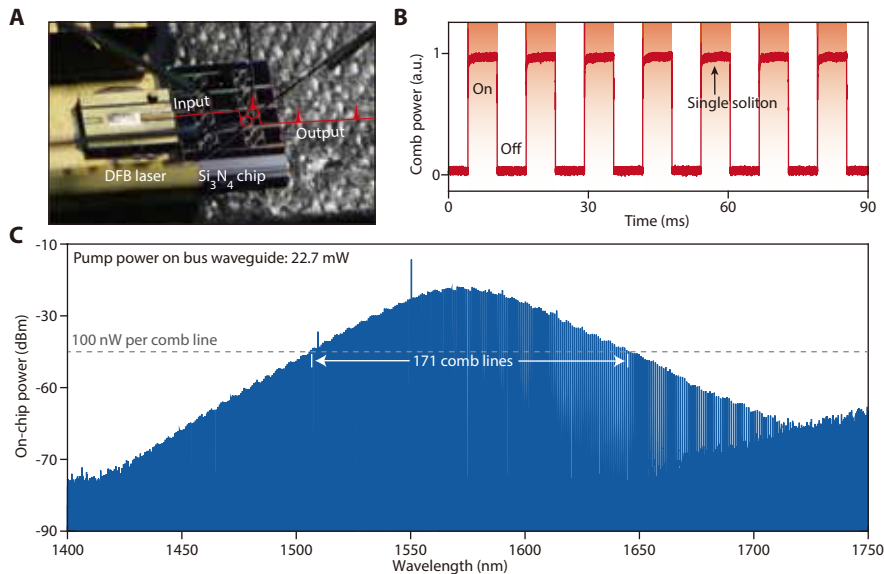


**Fig. 4. Hybrid-integrated soliton microcombs.** (A) Photo image showing a DFB laser directly coupled to a  $\text{Si}_3\text{N}_4$  chip. (b) Measured comb power when the laser is turned on and off for 7 consecutive times. (c) Optical spectrum of a single-soliton microcomb.

pump power while avoiding the MI regime. This is achieved by incrementally raising the NR’s resonant frequency while lowering that of the RC until their frequencies effectively swap (Fig. 2D). This maneuver shifts the effective pump curve, repositioning the soliton state to regimes of higher pump power and larger detuning. Following the swapping stage, we increase the NR’s resonant frequency, while the pump laser remains aligned close to the RC resonance (Fig. 2E). The increased detuning between the pump and the NR significantly broadens the soliton microcomb spectrum to an extent typically unattainable in waveguide-coupled devices.

Experimentally, we employ a probe laser to monitor the NR and RC frequencies during tuning (Fig. 3A). Coupled from either the through port or the drop port and collected at the input, the probe signal interrogates the hybridized resonances of the NR and RC. The frequency of the pump laser slowly increases for soliton generation. It is observed that single-soliton states are reliably generated in approximately 80% of trails (Fig. 3B). When solitons are generated, we scan the frequency of the probe laser and observe a narrow beatnote resulting from interference with backreflected pump (Fig. 3C). Broader peaks correspond to hybridized resonances from which the RC and NR resonant frequencies are deduced (see Supplementary Materials). A pump-NR detuning of 0.34 GHz yields a comb spanning 234 nm at -60 dBm power level. During the swapping phase, the RC mode frequency is reduced (via increased  $V_{\text{RC}}$ ) while the NR mode is simultaneously shifted (via decreased  $V_{\text{NR}}$ ). When their frequencies are aligned, the pump-NR detuning is 1.24 GHz, giving rise to a slightly broader spectrum spanning 488 nm (Fig. 3D). In the final tuning stage, only the NR frequency is further increased. As the RC

and NR become spectrally separated and their hybridization weakens, one of the hybridized resonances becomes less distinct in the probe signal. By finely adjusting the pump frequency, we observe a minimum in the transmitted power at the through port, indicating alignment with the hybridized resonance. When the pump-NR detuning reaches approximately 9 GHz, the comb is broadened to 937 nm (Fig. 3E).

### Hybrid integration

Finally, we use an on-chip laser to drive the soliton microcomb through an RC. A distributed-feedback (DFB) laser is coupled into the  $\text{Si}_3\text{N}_4$  chip, delivering approximately 20 mW of optical power to the bus waveguide after insertion losses (Fig. 4A). To enable operation at this low pump power, an NR with higher  $Q$  is selected (see Supplementary Materials). Without an optical isolator, light backscattered from the microresonator re-enters the laser cavity and perturbs its tuning. This phenomenon, known as self-injection locking<sup>29–32</sup>, narrows the laser’s linewidth and biases the system toward soliton microcomb generation when the feedback phase is appropriately tuned. In our implementation, the reinjection feedback phase is adjusted using a piezoelectric stage to meet the condition for stable soliton formation.

By optimizing the feedback phase, single-soliton microcombs emerge deterministically each time the laser current is tuned to a predetermined setpoint. To emulate soliton turn-on dynamics, the laser current is modulated with a square wave (Fig. 4B). Each time the current is switched to the target value, a single-soliton state reliably forms in the NR. Ultimately, this self-injection-locked pumping approach yields single-soliton microcombs with a 98.8 GHz FSR and an optical bandwidth exceeding 300

nm (Fig. 4C). 171 comb lines are above 100 nW. This is the broadest soliton microcombs at such FSR when pumped by on-chip lasers.

### Discussion and outlook

Our results represent the broadest soliton microcomb reported within this FSR among continuous-wave-pumped devices. Although the ideal enhancement factor indicates that an even broader comb is attainable at the present pump power, MI in the RC detrimentally impacts soliton stability, as confirmed by numerical simulations (see Supplementary Materials). Even if this limitation is overcome by degrading the RC quality factor, the maximal comb span is ultimately constrained by shifts in the spectral envelope center arising from Raman nonlinearity and dispersive-wave-induced spectral recoil<sup>4,33–36</sup>. These effects become increasingly significant as the spectrum broadens and must be carefully balanced to achieve octave-spanning combs<sup>37</sup>.

Moreover, the relatively high group-velocity dispersion in our device facilitates the generation of high-power comb lines. Even after amplification, these lines maintain the high signal-to-noise ratios necessary for telecommunications applications employing high-order modulation formats<sup>38,39</sup>. Consequently, when combined with the RC architecture, microresonators with exceptionally large dispersion can deliver numerous high-power comb

lines suitable for optical modules, potentially obviating the need for external optical amplifiers.

For the demonstrated ultra-broadband soliton microcomb, the total comb power collected at the drop port is 15.4 mW, corresponding to a conversion efficiency of 5.3%. This efficiency is partially limited by the high pump power (132 mW) that is directly transmitted and by the significant fraction of comb power (54 mW) that couples from the NR to the RC and escapes through the through port (see Supplementary Materials). Future improvements should focus on optimizing the dissipation rates and coupling parameters to approach the generalized critical coupling condition, thereby minimizing wasted pump power at the through port<sup>22,23,27</sup>. Moreover, the RC's resonant structures must be engineered so that coupling with the NR is confined to a single resonance. Notably, our configuration maintains the pump power used to initiate the soliton microcomb throughout its operation, unlike other methods that reduce pump power in the soliton regime to enhance conversion efficiency<sup>23</sup>. Consequently, the pump power employed here directly determines the laser power requirement. With the advent of high-power laser diodes, fully integrated soliton microcombs covering an ultra-broad wavelength range are now within reach<sup>29–32,40,41</sup>.

- 
- [1] Kippenberg, T. J., Gaeta, A. L., Lipson, M. & Gorodetsky, M. L. Dissipative Kerr solitons in optical microresonators. *Science* **361** (2018).
  - [2] Herr, T. *et al.* Temporal solitons in optical microresonators. *Nat. Photon.* **8**, 145–152 (2014).
  - [3] Yi, X., Yang, Q.-F., Yang, K. Y., Suh, M.-G. & Vahala, K. Soliton frequency comb at microwave rates in a high-Q silica microresonator. *Optica* **2**, 1078–1085 (2015).
  - [4] Brasch, V. *et al.* Photonic chip-based optical frequency comb using soliton Cherenkov radiation. *Science* **351**, 357–360 (2016).
  - [5] Spencer, D. T. *et al.* An optical-frequency synthesizer using integrated photonics. *Nature* **557**, 81–85 (2018).
  - [6] Newman, Z. L. *et al.* Architecture for the photonic integration of an optical atomic clock. *Optica* **6**, 680–685 (2019).
  - [7] Suh, M.-G., Yang, Q.-F., Yang, K. Y., Yi, X. & Vahala, K. J. Microresonator soliton dual-comb spectroscopy. *Science* **354**, 600–603 (2016).
  - [8] Dutt, A. *et al.* On-chip dual-comb source for spectroscopy. *Sci. Adv.* **4**, e1701858 (2018).
  - [9] Yang, Q.-F. *et al.* Vernier spectrometer using counter-propagating soliton microcombs. *Science* **363**, 965–968 (2019).
  - [10] Marin-Palomo, P. *et al.* Microresonator-based solitons for massively parallel coherent optical communications. *Nature* **546**, 274 (2017).
  - [11] Feldmann, J. *et al.* Parallel convolutional processing using an integrated photonic tensor core. *Nature* **589**, 52–58 (2021).
  - [12] Shu, H. *et al.* Microcomb-driven silicon photonic systems. *Nature* **605**, 457–463 (2022).
  - [13] Telle, H. R. *et al.* Carrier-envelope offset phase control: A novel concept for absolute optical frequency measurement and ultrashort pulse generation. *Appl. Phys. B* **69**, 327–332 (1999).
  - [14] Lesko, D. M. *et al.* A six-octave optical frequency comb from a scalable few-cycle erbium fibre laser. *Nat. Photon.* **15**, 281–286 (2021).
  - [15] Liang, Q., Bisht, A., Scheck, A., Schunemann, P. G. & Ye, J. Modulated ringdown comb interferometry for sensing of highly complex gases. *Nature* 1–8 (2025).
  - [16] Li, Q. *et al.* Octave-spanning microcavity kerr frequency combs with harmonic dispersive-wave emission on a silicon chip. In *Frontiers in Optics*, FW6C–5 (OSA, 2015).
  - [17] Drake, T. E. *et al.* Terahertz-rate kerr-microresonator optical clockwork. *Phys. Rev. X* **9**, 031023 (2019).
  - [18] Song, Y., Hu, Y., Zhu, X., Yang, K. & Lončar, M. Octave-spanning kerr soliton frequency combs in dispersion-and dissipation-engineered lithium niobate microresonators. *Light Sci. Appl.* **13**, 225 (2024).
  - [19] Del'Haye, P. *et al.* Phase-coherent microwave-to-optical link with a self-referenced microcomb. *Nat. Photon.* **10**, 516–520 (2016).
  - [20] Bao, C. *et al.* Nonlinear conversion efficiency in kerr frequency comb generation. *Opt. Lett.* **39**, 6126–6129 (2014).
  - [21] Yang, Q.-F., Hu, Y., Torres-Company, V. & Vahala, K. Efficient microresonator frequency combs. *eLight* **4**, 18 (2024).

- [22] Xue, X., Zheng, X. & Zhou, B. Super-efficient temporal solitons in mutually coupled optical cavities. *Nat. Photon.* **13**, 616–622 (2019).
- [23] Helgason, Ó. B. *et al.* Surpassing the nonlinear conversion efficiency of soliton microcombs. *Nat. Photon.* 1–8 (2023).
- [24] Obrzud, E., Lecomte, S. & Herr, T. Temporal solitons in microresonators driven by optical pulses. *Nat. Photon.* **11**, 600 (2017).
- [25] Anderson, M. H. *et al.* Zero dispersion kerr solitons in optical microresonators. *Nat. Commun.* **13**, 4764 (2022).
- [26] Li, J. *et al.* Efficiency of pulse pumped soliton microcombs. *Optica* **9**, 231–239 (2022).
- [27] Hu, Y. *et al.* High-efficiency and broadband on-chip electro-optic frequency comb generators. *Nat. Photon.* **16**, 679–685 (2022).
- [28] Wang, Y. *et al.* Compact turnkey soliton microcombs at microwave rates via wafer-scale fabrication. *arXiv preprint arXiv:2502.10941* (2025).
- [29] Liang, W. *et al.* High spectral purity Kerr frequency comb radio frequency photonic oscillator. *Nat. Commun.* **6**, 7957 (2015).
- [30] Raja, A. S. *et al.* Electrically pumped photonic integrated soliton microcomb. *Nat. Commun.* **10**, 680 (2019).
- [31] Shen, B. *et al.* Integrated turnkey soliton microcombs. *Nature* **582**, 365–369 (2020).
- [32] Jin, W. *et al.* Hertz-linewidth semiconductor lasers using cmos-ready ultra-high-Q microresonators. *Nat. Photon.* **15**, 346–353 (2021).
- [33] Karpov, M. *et al.* Raman self-frequency shift of dissipative kerr solitons in an optical microresonator. *Phys. Rev. Lett.* **116**, 103902 (2016).
- [34] Yi, X., Yang, Q.-F., Yang, K. Y. & Vahala, K. Theory and measurement of the soliton self-frequency shift and efficiency in optical microcavities. *Opt. Lett.* **41**, 3419–3422 (2016).
- [35] Yi, X. *et al.* Single-mode dispersive waves and soliton microcomb dynamics. *Nat. Commun.* **8**, 14869 (2017).
- [36] Wang, Y., Anderson, M., Coen, S., Murdoch, S. G. & Erkintalo, M. Stimulated raman scattering imposes fundamental limits to the duration and bandwidth of temporal cavity solitons. *Phys. Rev. Lett.* **120**, 053902 (2018).
- [37] Skryabin, D., Luan, F., Knight, J. & Russell, P. S. J. Soliton self-frequency shift cancellation in photonic crystal fibers. *Science* **301**, 1705–1708 (2003).
- [38] Jørgensen, A. *et al.* Petabit-per-second data transmission using a chip-scale microcomb ring resonator source. *Nat. Photon.* 1–5 (2022).
- [39] Zhang, C. *et al.* Clone-comb-enabled high-capacity digital-analogue fronthaul with high-order modulation formats. *Nat. Photon.* **17**, 1000–1008 (2023).
- [40] Stern, B., Ji, X., Okawachi, Y., Gaeta, A. L. & Lipson, M. Battery-operated integrated frequency comb generator. *Nature* **562**, 401 (2018).
- [41] Xiang, C. *et al.* Laser soliton microcombs heterogeneously integrated on silicon. *Science* **373**, 99–103 (2021).

## Acknowledgments

This work was supported by Beijing Natural Science Foundation (Z210004) and National Natural Science Foundation of China (92150108). The authors thank Jincheng Li, Zhigang Hu, Hao Yang, Ruokai Zheng, and Xiaoxuan Peng for assistance in fabrication. The fabrication in this work was supported by the Peking University Nano-Optoelectronic Fabrication Center, Micro/nano Fabrication Laboratory of Synergetic Extreme Condition User Facility (SECUF), Songshan Lake Materials Laboratory, and the Advanced Photonics Integrated Center of Peking University.

## Author contributions

Experiments were conceived and designed by X.Z., X.L., and Q.-F.Y. Measurements and data analysis were performed by X.Z., X.L., with assistance from Z.W. and T.X. Numerical simulations were performed by X.Z., and X.L. The device was designed by K.Z. and X.L. with assistance from Y.L. The device was fabricated by Y.W., with assistance from Y.C., J.W., H.L., X.Z., M.W., J.-F.L., X.C., T.W., and B.-B.L. The project was supervised by Q.G. and Q.-F.Y. All authors participated in preparing the manuscript.

## Competing interests

The authors declare no competing interests.

## Data availability

The data that support the plot within this paper and other findings of this study are available upon publication.

## Code availability

The codes that support the findings of this study are available upon publication.

## Additional information

Correspondence and requests for materials should be addressed to Q.-F.Y.

# Supplementary information: Ultra-broadband soliton microcombs in resonantly-coupled microresonators

Kaixuan Zhu<sup>1\*</sup>, Xinrui Luo<sup>1\*</sup>, Yuanlei Wang<sup>1,2\*</sup>, Ze Wang<sup>1\*</sup>, Tianyu Xu<sup>1</sup>, Du Qian<sup>1</sup>, Yinke Cheng<sup>1,2</sup>, Junqi Wang<sup>1</sup>, Haoyang Luo<sup>1</sup>, Yanwu Liu<sup>1</sup>, Xing Jin<sup>1</sup>, Xin Zhou<sup>2</sup>, Min Wang<sup>2</sup>, Jian-Fei Liu<sup>2</sup>, Xuening Cao<sup>2</sup>, Ting Wang<sup>2</sup>, Qihuang Gong<sup>1,3,4</sup>, Bei-Bei Li<sup>2</sup>, and Qi-Fan Yang<sup>1,3,4†</sup>

<sup>1</sup>State Key Laboratory for Artificial Microstructure and Mesoscopic Physics and Frontiers Science Center for Nano-optoelectronics, School of Physics, Peking University, Beijing 100871, China

<sup>2</sup>Beijing National Laboratory for Condensed Matter Physics, Institute of Physics, Chinese Academy of Sciences, Beijing 100190, China

<sup>3</sup>Peking University Yangtze Delta Institute of Optoelectronics, Nantong, Jiangsu 226010, China

<sup>4</sup>Collaborative Innovation Center of Extreme Optics, Shanxi University, Taiyuan 030006, China

\*These authors contributed equally to this work.

†Corresponding author: leonardoyoung@pku.edu.cn

(Dated: March 5, 2025)

## CONTENTS

I. Theory	2
A. Simplified model and master equations	2
B. Effective pump power	2
C. Phase diagrams	3
D. Soliton existence range	5
E. Effective pump power in the modulation instability regime	5
F. Complete model for coupled resonators	6
II. Device fabrication and characterization	7
A. Fabrication process	7
B. Dispersion	7
C. Quality factors	8
D. Resonant frequencies	9
III. Additional Characterization of Microcombs	10
A. Optical spectrum	10
B. Autocorrelation	11
C. Coherence	11
References	12



## I. THEORY

### A. Simplified model and master equations

We consider a system comprising two coupled microresonators. The first is a single-mode linear resonant coupler microresonator (RC), which we assume supports only one mode. The second is a broadband nonlinear resonator (NR) described by the Lugiato–Lefever equation (LLE). A set of equations describes their coupled dynamics:

$$\frac{\partial b_0}{\partial T} = -\frac{\kappa_{\text{RC}}}{2}b_0 - i\delta\omega_{\text{RC}}b_0 + iGa_0 + \sqrt{\frac{\kappa_{\text{e,RC}}P_{\text{in}}}{\hbar\omega_0}}, \quad (\text{S1})$$

$$\frac{\partial A}{\partial T} = -\frac{\kappa_{\text{NR}}}{2}A - i\delta\omega_{\text{NR}}A + i\frac{D_{2,\text{NR}}}{2}\frac{\partial^2 A}{\partial\phi^2} + ig_{\text{NR}}|A|^2A + iGb_0, \quad (\text{S2})$$

where  $T$  is the slow time (lab time) and  $\phi$  is the angular coordinate in the moving frame.  $b_0$  represents the field amplitude in  $0_{\text{th}}$  mode of the RC and  $A(T, \phi)$  corresponds to the slowly varying field amplitude of the nonlinear resonator (NR). These quantities are normalized such that  $|b_0|^2$  and  $|A|^2$  correspond to the intracavity photon number.  $D_{2,\text{NR}}$  is the second-order dispersion in the NR. The decay rates of NR and RC are defined as  $\kappa_{\text{NR}} = \kappa_{0,\text{NR}} + \kappa_{\text{e,NR}}$ ,  $\kappa_{\text{RC}} = \kappa_{0,\text{RC}} + \kappa_{\text{e,RC}}$ , where  $\kappa_{0,\text{NR}}$ ,  $\kappa_{0,\text{RC}}$  are the intrinsic decay rates and  $\kappa_{\text{e,NR}}$ ,  $\kappa_{\text{e,RC}}$  represent the coupling to the waveguide. The nonlinear coefficient of the NR is defined as  $g_{\text{NR}} = \hbar\omega_0^2cn_2/n_0^2V_{\text{eff,NR}}$ , where  $V_{\text{eff,NR}}$  is the effective mode volume and  $n_2$  is the nonlinear refractive index associated with the refractive index  $n_0$ . The coupling strength between the microresonators is given by a real number  $G$ .  $\delta\omega_{\text{RC(NR)}}$  represent the pump-RC (NR) detuning.  $P_{\text{in}}$  is the pump power on the RC.

For convenience, we normalize the coupled LLE as follows:

$$\frac{\partial\psi_{\text{RC}}}{\partial\tau} = -(\kappa_{\text{r}} + i\zeta_{\text{RC}})\psi_{\text{RC}} + ig_c\psi_{0,\text{NR}} + f_{\text{p}}, \quad (\text{S3})$$

$$\frac{\partial\psi_{\text{NR}}}{\partial\tau} = -(1 + i\zeta_{\text{NR}})\psi_{\text{NR}} + id_{2,\text{NR}}\frac{\partial^2\psi_{\text{NR}}}{\partial\phi^2} + i|\psi_{\text{NR}}|^2\psi_{\text{NR}} + ig_c\psi_{\text{RC}}. \quad (\text{S4})$$

Here,  $\tau = \frac{\kappa_{\text{NR}}}{2}T$ ,  $A = \sqrt{\frac{\kappa_{\text{NR}}}{2g_{\text{NR}}}}\psi_{\text{NR}}$ ,  $b_0 = \sqrt{\frac{\kappa_{\text{NR}}}{2g_{\text{NR}}}}\psi_{\text{RC}}$ ,  $a_0 = \sqrt{\frac{\kappa_{\text{NR}}}{2g_{\text{NR}}}}\psi_{0,\text{NR}}$ ,  $\zeta_{\text{NR}} = \frac{2\delta\omega_{\text{NR}}}{\kappa_{\text{NR}}}$ ,  $\zeta_{\text{RC}} = \frac{2\delta\omega_{\text{RC}}}{\kappa_{\text{NR}}}$ ,  $\kappa_{\text{r}} = \frac{\kappa_{\text{RC}}}{\kappa_{\text{NR}}}$ ,  $g_c = \frac{2G}{\kappa_{\text{NR}}}$ ,  $d_{2,\text{NR}} = \frac{D_{2,\text{NR}}}{\kappa_{\text{NR}}}$ ,  $f_{\text{p}} = \sqrt{\frac{8g_{\text{NR}}\kappa_{\text{e,RC}}P_{\text{in}}}{\kappa_{\text{NR}}^3\hbar\omega_0}}$ . Notably, the normalized pump power on RC can be described as

$$f_{\text{p}}^2 = \frac{P_{\text{in}}}{P_{\text{th,NR}}} \cdot \frac{\kappa_{\text{e,RC}}}{\kappa_{\text{e,NR}}}. \quad (\text{S5})$$

Here,  $P_{\text{th,NR}}$  represents the parametric oscillation threshold of NR when coupled from the bus waveguide and is defined as  $P_{\text{th,NR}} = \frac{\hbar\omega_0\kappa_{\text{NR}}^3}{8g_{\text{NR}}\kappa_{\text{e,NR}}}$ .

### B. Effective pump power

We define the effective pump term  $f_{\text{eff}} = ig_c\psi_{\text{RC}}$ , such that Eq. S4 yields the standard form of the LLE. An estimation for  $f_{\text{eff}}^2$  can be obtained by considering the steady-state continuous-wave (CW) solution of the coupled LLE. The optical field of the  $0_{\text{th}}$  mode of the NR is given by

$$\psi_{0,\text{NR}} \approx \frac{ig_c\psi_{\text{RC}}}{1 + i\zeta_{\text{NR}}}. \quad (\text{S6})$$

Inserting it into Eq. S3 and considering  $\frac{\partial\psi_{\text{RC}}}{\partial\tau} = 0$  yields:

$$f_{\text{p}} = (\kappa_{\text{r}} + i\zeta_{\text{RC}})\psi_{\text{RC}} + \frac{g_c^2}{1 + i\zeta_{\text{NR}}}\psi_{\text{RC}}. \quad (\text{S7})$$

Taking the modulus, we obtain the intracavity power of RC:

$$|\psi_{\text{RC}}|^2 = \frac{f_{\text{p}}^2}{\left(\kappa_{\text{r}} + \frac{g_{\text{c}}^2}{1+\zeta_{\text{NR}}^2}\right)^2 + \left(\zeta_{\text{RC}} - \frac{g_{\text{c}}^2\zeta_{\text{NR}}}{1+\zeta_{\text{NR}}^2}\right)^2}. \quad (\text{S8})$$

Thus, the effective pump power for the NR is given by

$$|f_{\text{eff}}^2| = g_{\text{c}}^2 |\psi_{\text{RC}}|^2 = \frac{g_{\text{c}}^2 f_{\text{p}}^2}{\left(\kappa_{\text{r}} + \frac{g_{\text{c}}^2}{1+\zeta_{\text{NR}}^2}\right)^2 + \left(\zeta_{\text{RC}} - \frac{g_{\text{c}}^2\zeta_{\text{NR}}}{1+\zeta_{\text{NR}}^2}\right)^2}. \quad (\text{S9})$$

As the system transitions to the soliton state, large detuning in the NR causes,  $\frac{g_{\text{c}}^2}{1+\zeta_{\text{NR}}^2} \rightarrow 0$ , and the effective pump power converges to,

$$|f_{\text{eff}}^2| = \frac{g_{\text{c}}^2 f_{\text{p}}^2}{\kappa_{\text{r}}^2 + \zeta_{\text{RC}}^2}. \quad (\text{S10})$$

We can see that the effective pump power is maximized when the pump is resonant with the RC ( $\zeta_{\text{RC}} = 0$ ). Under this condition, the optimized effective pump power is given by:

$$|f_{\text{eff}}^2| = \frac{g_{\text{c}}^2 f_{\text{p}}^2}{\kappa_{\text{r}}^2}. \quad (\text{S11})$$

To compare the effective pump power delivered to the NR employing RC with the case using waveguide couplers, we consider the same pump power  $P_{\text{in}}$  launched on the waveguide coupler, with a coupling rate of  $\kappa_{\text{e,NR}}$ . Thus, the normalized pump power for the NR using the waveguide coupler is defined as

$$f^2 = \frac{P_{\text{in}}}{P_{\text{th,NR}}}. \quad (\text{S12})$$

Therefore, the enhancement factor for RC coupling relative to waveguide coupling is given by

$$\Gamma = \frac{|f_{\text{eff}}^2|}{f^2}. \quad (\text{S13})$$

According to Eq. S11, Eq. S12 and Eq. S5, the enhancement factor can be calculated by

$$\Gamma = \frac{4G^2}{\kappa_{\text{NR}}\kappa_{\text{RC}}} \cdot \frac{\eta_{\text{RC}}}{\eta_{\text{NR}}}. \quad (\text{S14})$$

The loading factors  $\eta_{\text{NR(RC)}} = \kappa_{\text{e,NR(RC)}}/\kappa_{\text{NR(RC)}}$ . For efficiency coupling, they are usually in the range between 0.5 to 1. Therefore, the ratio  $\frac{\eta_{\text{RC}}}{\eta_{\text{NR}}}$  is in the order of unity, and the enhancement factor is on the order of

$$\Gamma \approx \frac{4G^2}{\kappa_{\text{NR}}\kappa_{\text{RC}}}. \quad (\text{S15})$$

### C. Phase diagrams

Numerical simulations of the coupled Lugiato–Lefever equation are performed using the Split-Step Fourier Transform method with 1024 modes. Each mode is initially seeded with half the energy of a single photon. The normalized coefficients employed in fig. S1 are:  $k_{\text{r}} = 6.52$ ,  $g_{\text{c}} = 18.35$ , and  $d_{2,\text{NR}} = -0.004$ .

We present the simulated evolution of states within the phase diagram, which delineates the emergence of nonlinear behavior in the NR. In fig. S1A, the black trajectory represents the theoretical trace derived from the analytical model, while the gray trajectory depicts the simulated RC intracavity field scaled by  $g_{\text{c}}^2$ , corresponding to the effective pump power  $f_{\text{eff}}^2$ . Notably, transitioning from the continuous-wave (CW) state to the soliton state necessitates a reverse laser scan. As the system nears the boundary of the monostable modulation instability (MI) regime, the RC intracavity field experiences an abrupt drop at the MI-soliton boundary, followed by oscillations in its vicinity—a

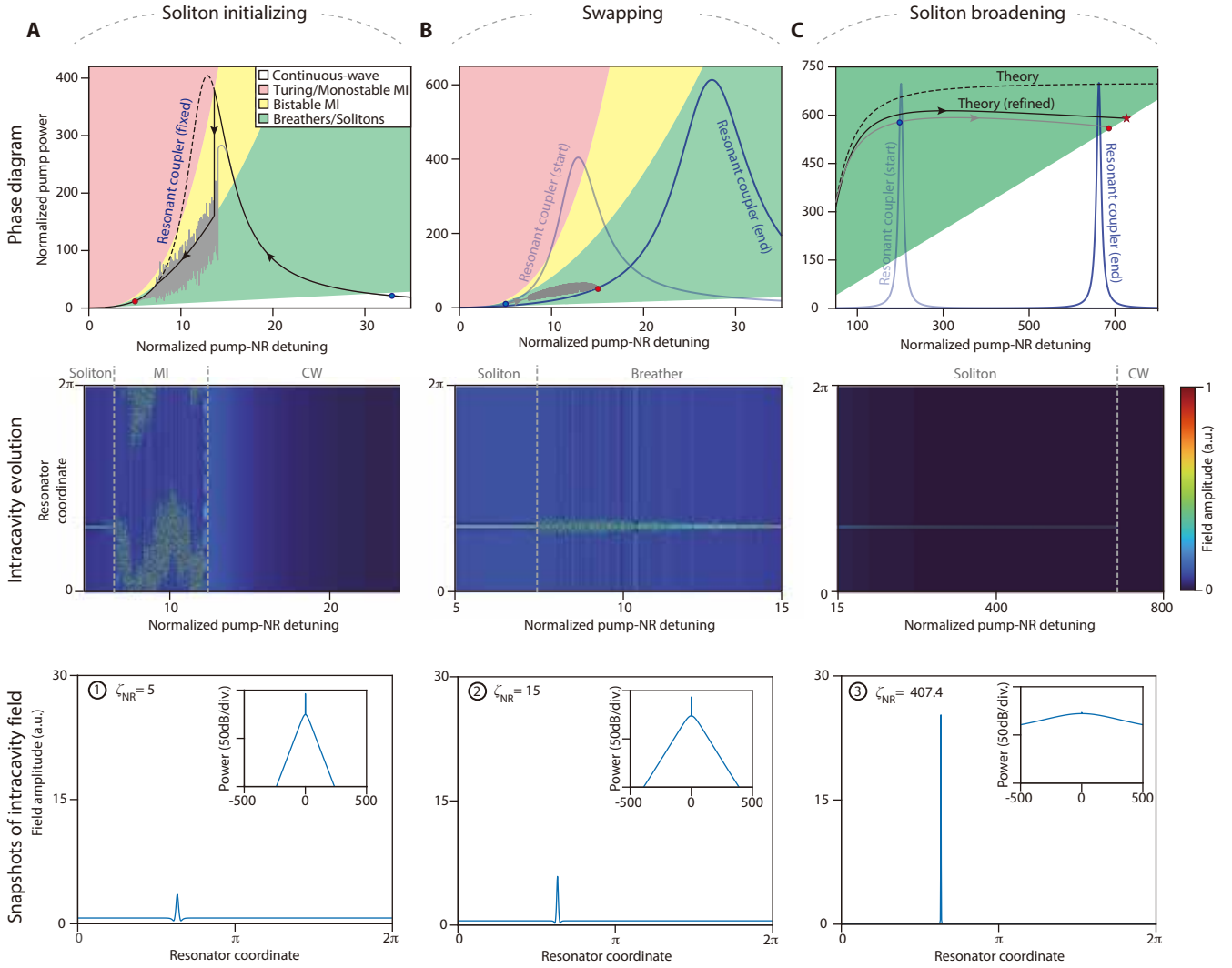


**Fig. S1. Theoretical and simulated pathways to soliton formation in phase diagrams.** (A–C) Sequential stages for generating ultra-broadband solitons in a resonantly-coupled NR. Top panels: corresponding trajectories in the NR phase diagram. The blue curve represents the effective pump power delivered through the RC. The black and gray trajectories represent the theoretical prediction and simulated evolution of the effective pump power during tuning, respectively. The simulated tuning trace begins and ends at the blue and red dots. The black dashed and solid curves in (C) represent the tuning traces predicted by the theory and the refined theory, respectively. The maximum detuning predicted by the refined theory is marked by the red star. Middle panels: temporal evolution of the intracavity field. Bottom panels: snapshots of the intracavity field at different NR-pump detunings, also marked as red dots in the third panel. Insets: optical spectra.

phenomenon that is discussed in greater detail later. The MI state persists until the effective pump power falls below the critical threshold, resulting in the formation of a single soliton, as illustrated in fig. S1A.

Upon establishing the soliton state, we start the swap operation by gradually tuning the RC resonance toward the pump laser. In this process, the frequency of the NR should be adjusted to ensure that the NR remains in the soliton or breather state (fig. S1B). After the swap, the effective pump power may not have reached its maximum; however, in the subsequent soliton broadening stage, tuning the NR mode further into the far red-detuned regime can also help approach the maximum effective pump power according to Eq. S9. This simplifies the tuning process in the soliton broadening stage and is visualized in fig. S1C.

#### D. Soliton existence range

As discussed in previous works<sup>1,2</sup>, the relationship between soliton detuning and pumping in a regular LLE is given by  $\zeta \leq \frac{\pi^2 f^2}{8}$ . Thus, for devices with RC, the maximum detuning range of the soliton is given by:

$$\zeta_{\text{NR}} \leq \frac{\pi^2 |f_{\text{eff}}^2|}{8} = \Gamma \frac{\pi^2 f^2}{8}. \quad (\text{S16})$$

Therefore, compared with waveguide-coupled NRs, in resonantly-coupled NRs the accessible detuning for soliton states is increased by a factor of  $\Gamma$ . However, as illustrated in fig. S1, when the detuning of the NR becomes large, a notable decrease of the effective pump power occurs. This requires additional correction that applies to the intracavity field of the NR (Eq. S6), with contribution from the 0th mode spectral component of the soliton. Adding it to the continuous-wave background yields

$$\psi_{0,\text{NR}} = \sqrt{\frac{d_{2,\text{NR}}}{2}} e^{i\varphi} + \frac{ig_c \psi_{\text{RC}}}{1 + i\zeta_{\text{NR}}} \approx \sqrt{\frac{d_{2,\text{NR}}}{2}} e^{i\varphi} + \frac{g_c \psi_{\text{RC}}}{\zeta_{\text{NR}}}. \quad (\text{S17})$$

where  $\sqrt{\frac{d_{2,\text{NR}}}{2}} e^{i\varphi}$  corresponds to the 0th mode spectral component of the soliton and  $\varphi$  corresponds to the phase of the soliton. At small detuning, the first term is negligible compared with the second term. However, at large detuning, its contribution should be considered. Substituting Eq. S17 into Eq. S3 and considering  $\frac{\partial \psi_{\text{RC}}}{\partial \tau} = 0$  yields:

$$f_p + ig_c \sqrt{\frac{d_{2,\text{NR}}}{2}} e^{i\varphi} = (\kappa_r + i\zeta_{\text{RC}}) \psi_{\text{RC}} + \frac{g_c^2}{1 + i\zeta_{\text{NR}}} \psi_{\text{RC}}. \quad (\text{S18})$$

Taking the modulus of both sides gives:

$$|\psi_{\text{RC}}|^2 = \frac{(f_p - g_c \sqrt{\frac{d_{2,\text{NR}}}{2}} \sin \varphi)^2 + g_c^2 \frac{d_{2,\text{NR}}}{2} \cos^2 \varphi}{(\kappa_r + \frac{g_c^2}{1 + \zeta_{\text{NR}}})^2 + (\zeta_{\text{RC}} - \frac{g_c^2 \zeta_{\text{NR}}}{1 + \zeta_{\text{NR}}})^2}. \quad (\text{S19})$$

As the detuning becomes large enough to approach its maximum, we find that  $\sin \varphi$  approaches 1, and  $\cos \varphi$  tends to 0<sup>2</sup>:

$$\sin \varphi = \sqrt{\frac{8\zeta_{\text{NR}}}{\pi^2 g_c^2 |\psi_{\text{RC}}|^2}} \rightarrow 1, \cos \varphi \rightarrow 0. \quad (\text{S20})$$

Therefore, the effective pump power for large detuning is modified to:

$$|f_{\text{eff}}^2| = g_c^2 |\psi_{\text{RC}}|^2 \approx g_c^2 \frac{(f_p - g_c \sqrt{\frac{d_{2,\text{NR}}}{2}})^2}{\kappa_r^2}, \quad (\text{S21})$$

which further gives the modified the soliton existence range:

$$\zeta_{\text{NR}} \leq \frac{\pi^2 g_c^2 (f_p - g_c \sqrt{\frac{d_{2,\text{NR}}}{2}})^2}{8 \kappa_r^2}. \quad (\text{S22})$$

As shown in fig. S1C, this refined theory exhibits a better agreement with numerical simulations.

#### E. Effective pump power in the modulation instability regime

The derivation above, which employs the coupled LLEs under steady CW conditions, captures the key physics of our system. However, this description assumes that the NR remains in either the CW or soliton state, where the intracavity field is well approximated by the steady-state solution. In MI regime, this assumption breaks down, as no well-defined steady-state solution exists for the intracavity field, making it difficult to directly determine  $f_{\text{eff}}$  using the previous approach. Nevertheless, simulations show that once parametric oscillation sets in, the zero-mode energy

$|\psi_{0,\text{NR}}|^2$  in the NR fluctuates around 1. This allows us to approximate  $f_{\text{eff}}$  as follows,

$$f_{\text{eff}}^2 \approx 1 + (\zeta_{\text{NR}} - 1)^2 \quad (\text{S23})$$

Coincidentally, this line also corresponds to the boundary that separates the MI and soliton regions in the single-cavity phase diagram<sup>3,4</sup>. Therefore, as illustrated by the gray line in fig. S1, when the field of NR enters the MI region, its trajectory oscillates around this boundary.

### F. Complete model for coupled resonators

Our theoretical analysis and simulations above assume that the RC behaves as a single-mode linear microresonator. However, the RC may also exhibit significant nonlinearity and dispersion. We therefore present a comprehensive model that accounts not only for the RC's dispersion and nonlinearity but also for Raman effects and higher-order dispersion in the NR:

$$\frac{\partial A}{\partial T} = \mathcal{F} \left[ i \left( -\delta\omega_{\text{NR}} A + D_{\text{int,NR}}(\mu) \tilde{A}_\mu \right) \right] - \frac{\kappa_{\text{NR}}}{2} A + ig_{\text{NR}} |A|^2 A - ig \tau_{\text{R}} A \frac{\partial |A|^2}{\partial t} + iGB, \quad (\text{S24})$$

$$\frac{\partial B}{\partial T} = \mathcal{F} \left[ i \left( -\delta\omega_{\text{RC}} B + D_{\text{int,RC}}(\mu) \tilde{B}_\mu \right) \right] - \frac{\kappa_{\text{RC}}}{2} B + ig_{\text{RC}} |B|^2 B + iGA + \sqrt{\frac{\kappa_{\text{e,RC}} P_{\text{in}}}{\hbar\omega_0}}. \quad (\text{S25})$$

To simulate the optical spectra of the ultra-broadband soliton microcomb presented in the main text, we use the following parameters:  $Q_{0,\text{NR}} = 6.48$  M,  $Q_{\text{e,NR}} = 3.81$  M,  $Q_{0,\text{RC}} = 6.75$  M,  $Q_{\text{e,RC}} = 0.38$  M,  $g_{\text{NR}} = 1.37$  Hz,  $g_{\text{RC}} = 1.25$  Hz,  $G = 2\pi \times 1.65$  GHz, and  $\tau_{\text{R}} = 0.45$  fs. The wavelength-dependent coupling to the waveguide is determined from finite-element simulations.

The maximum pump–NR detuning supported in our device is approximately 10.7 GHz. Increasing the detuning beyond this limit induces modulation instability in the RC (fig. S2), which can cause fluctuation in its resonant frequency due to thermal nonlinearity. In the experiment, it could destabilize the soliton microcombs in the NR.

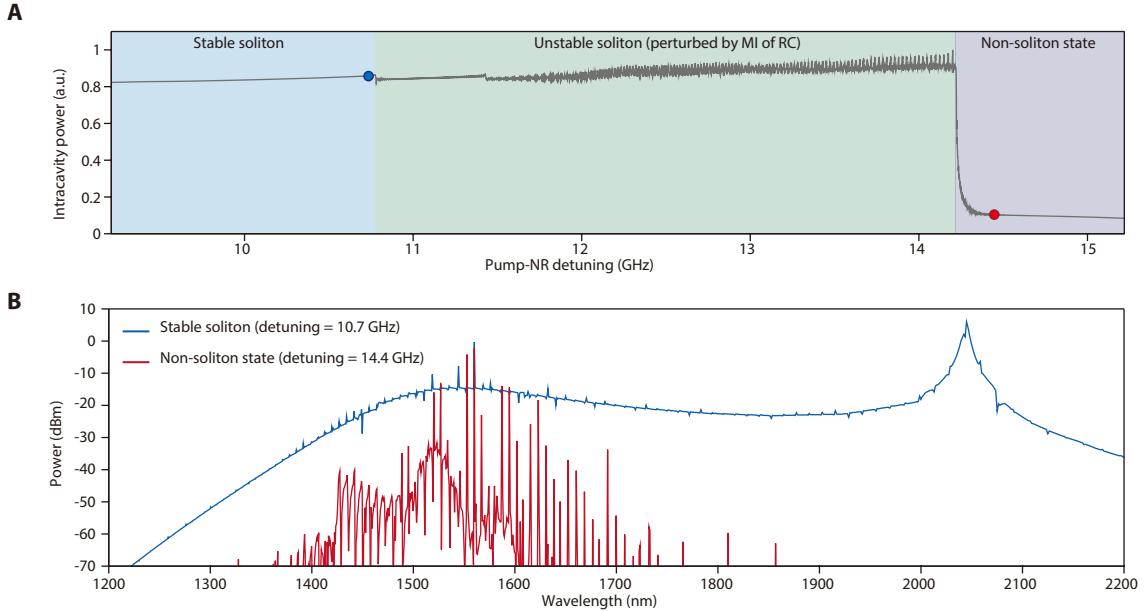


**Fig. S2. Simulation of ultra-broadband soliton microcombs based on the complete model.** (A) Evolution of intracavity power as the pump–NR detuning is increased. (B) Simulated optical spectra of the soliton state and non-soliton state indicated in A.

## II. DEVICE FABRICATION AND CHARACTERIZATION

### A. Fabrication process

The  $\text{Si}_3\text{N}_4$  coupled microresonators are fabricated on a 4-inch wafer through a series of subtractive processes<sup>5</sup>. The fabrication flow is illustrated in fig. S3A. Initially, a 786 nm thick  $\text{Si}_3\text{N}_4$  film is deposited in two steps onto a wet-oxidized silicon substrate featuring stress-release patterns. Electron beam lithography is used to define the pattern, followed by dry etching to transfer the resist pattern to the  $\text{Si}_3\text{N}_4$  film. The wafer is then annealed at 1200°C to remove residual N-H and Si-H bonds from the  $\text{Si}_3\text{N}_4$  film.  $\text{SiO}_2$  cladding is deposited, followed by a second annealing step for densifying the film. A lift-off process is then used to define the heater patterns. The wafer (fig. S3B) is diced into  $\text{Si}_3\text{N}_4$  chips. Their optical image and scanning electron microscopy image are shown in figs. S3C-D.

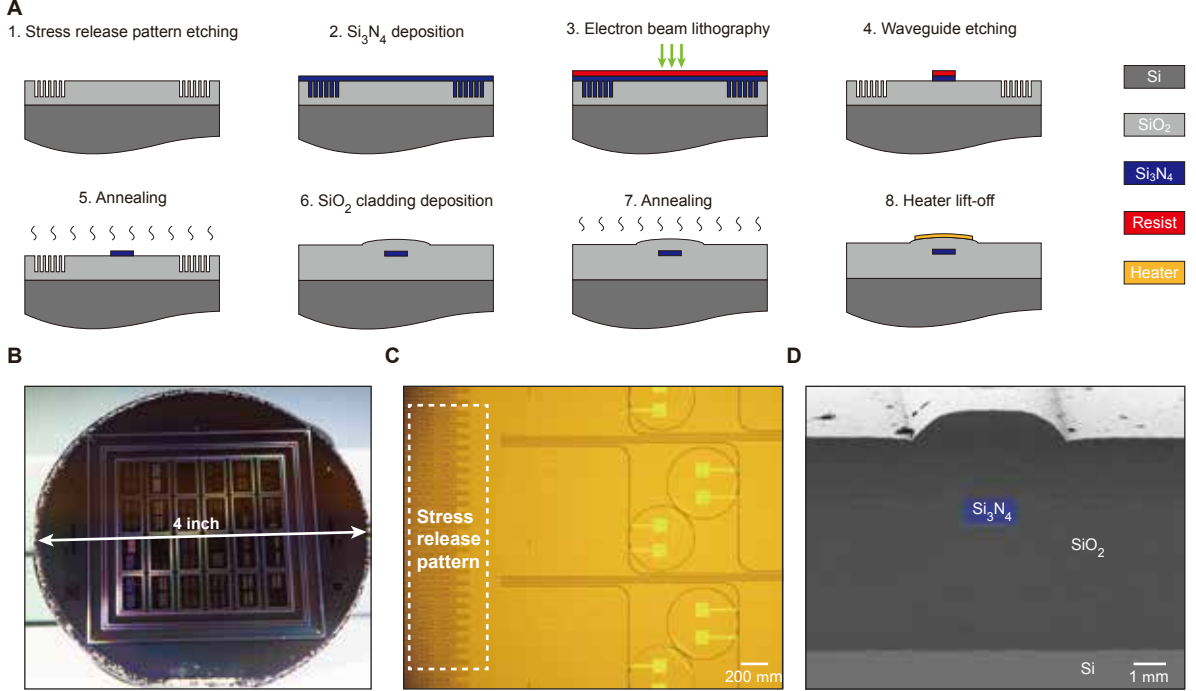


**Fig. S3. Fabrication process of coupled  $\text{Si}_3\text{N}_4$  microresonators.** (A) Schematic of the wafer-scale subtractive fabrication process flow. (B) The fully processed 4-inch wafer. (C) Optical micrograph of the  $\text{Si}_3\text{N}_4$  chip, with stress-release patterns highlighted by the white dashed box. (D) Cross-sectional scanning electron micrographs of the final chip.

### B. Dispersion

The dispersion of the microresonators is measured by sweeping several widely tunable lasers (Toptica CTL series) across the resonances while recording the transmission signal with a photodetector. To precisely calibrate the resonant frequencies of the modes in the microresonator, a portion of the laser power is split before entering the microresonator and sent through an unbalanced Mach-Zehnder interferometer (UMZI). The UMZI generates a sinusoidal transmission response as a function of frequency, serving as a reference for frequency calibration. The FSR and dispersion of the UMZI in each spectral band are calibrated using a fiber-cavity-based vector spectrum analyzer<sup>6</sup>.

The integrated dispersion is given by

$$D_{\text{int}}(\mu) = \omega_{\mu} - \omega_0 - \mu D_1 = \sum_{n \geq 2} D_n \mu^n / n! \quad (\text{S26})$$

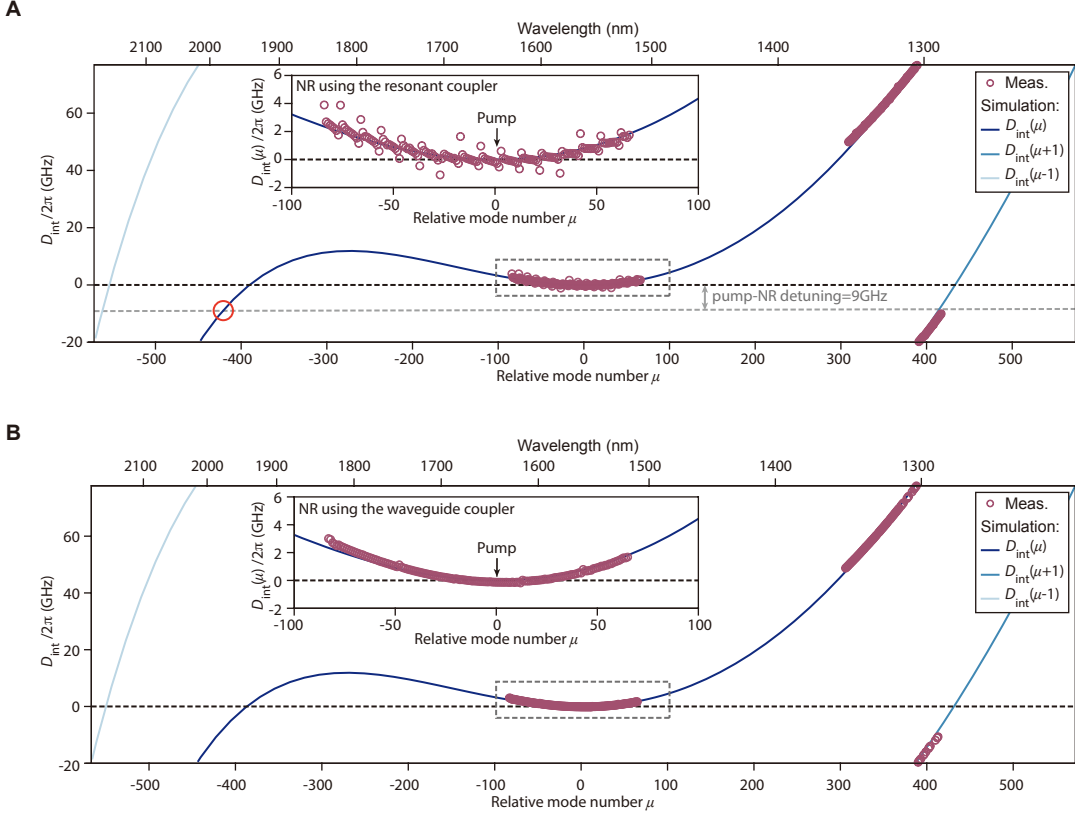


**Fig. S4. Mode family dispersion.** (A) The integrated dispersion of the NR using the resonant coupler. The pump-NR detuning is marked by the gray dashed line. The phase-matched location of the dispersive wave is marked by the red circle. (B) The integrated dispersion of the NR using the waveguide coupler. The measured and simulated  $D_{\text{int}}$  values are denoted by purple circles and blue curves, respectively.  $D_{\text{int}}(\mu)$  and its shifted values  $D_{\text{int}}(\mu \pm 1) = D_{\text{int}}(\mu) \mp D_1$  are represented in three distinct shades of blue. Insets: zoom-in view of  $D_{\text{int}}(\mu)$  values near the pump frequency.

where  $\omega_\mu$  is the resonant frequency of the  $\mu_{\text{th}}$  mode, and  $D_1$  is the FSR in angular frequency. By fitting the measured resonant frequencies with a fourth-degree polynomial, we extract the FSR:  $D_1/2\pi = 96.9$  GHz and dispersion parameters:  $D_2/2\pi = 821$  kHz,  $D_3/2\pi = -5.5$  kHz,  $D_4/2\pi = 107.7$  Hz for the NR using RC, while for the NR using waveguide coupler, the corresponding values are  $D_1/2\pi = 97.8$  GHz,  $D_2/2\pi = 858.2$  kHz,  $D_3/2\pi = -1$  kHz,  $D_4/2\pi = 34.4$  Hz. The FSR difference results from the slight variation in ring radii (232  $\mu\text{m}$  vs. 230  $\mu\text{m}$ ). However, the second-order dispersion ( $D_2$ ) remains similar, ensuring that under identical pump power, a comparison of soliton spectral bandwidth between the two kinds of microresonators is valid.

To investigate soliton-induced dispersive radiations, we perform finite element simulations of broadband dispersion, based on waveguide geometries with an upper base width of 1.8  $\mu\text{m}$ , a sidewall angle of  $85^\circ$ , a waveguide height of 800 nm, and ring radius of 232  $\mu\text{m}$  and 230  $\mu\text{m}$  for NR with resonant coupler and waveguide coupler, respectively. Simulated dispersions as well as experimental measurements are shown in fig. S4. Given an experimental detuning of approximately 9 GHz, we highlight  $D_{\text{int}}(\mu)/2\pi = -9$  GHz (red circle in fig. S4) to indicate the phase-matching condition for dispersive wave generation around 2000 nm. The predicted dispersive wave location does not match perfectly with the experiment, which can be attributed to the Raman effect and residual difference between the simulated and actual dispersion profiles (fig. S7).

### C. Quality factors

The quality factors of the waveguide-coupled NR for soliton generation in Fig. 1G are presented in fig. S5, which is close to that of the resonantly-coupled NR. Also, the quality factors of the RC and NR for hybrid-integrated soliton microcombs are presented in fig. S6. The NR here has a much higher quality factor due to a wider waveguide width and a reduced coupling to the bus waveguide.

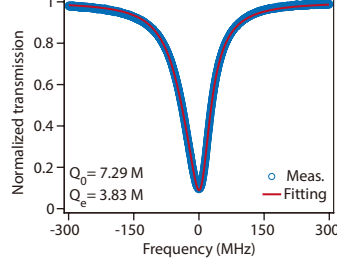


**Fig. S5. Measured transmission spectra of the NR using the waveguide coupler.** The NR is used for soliton generation in Fig. 1G in the maintext.

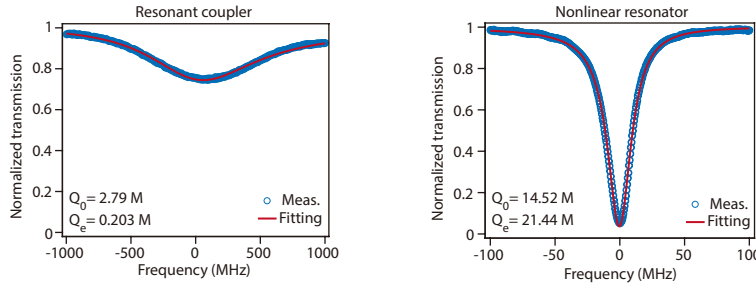


**Fig. S6. Measured transmission spectra of the RC and NR for hybrid-integrated soliton microcombs.** The  $\text{Si}_3\text{N}_4$  film has a thickness of 777 nm. The RC, with a width of 1  $\mu\text{m}$ , is overcoupled to suppress undesired parametric oscillations and broaden its resonance linewidth. The NR, designed for low-power operation, has a width of 2.5  $\mu\text{m}$  and is undercoupled.

#### D. Resonant frequencies

The hybridization of the pump resonances in the NR and RC is described by the following coupled equations:

$$\frac{\partial b_0}{\partial T} = -\frac{\kappa_{\text{RC}}}{2}b_0 - i\delta\omega_{\text{RC}}b_0 + iGa_0 + \sqrt{\kappa_{e,\text{RC}}}s_{\text{in}}, \quad (\text{S27})$$

$$\frac{\partial a_0}{\partial T} = -\frac{\kappa_{\text{NR}}}{2}a_0 - i\delta\omega_{\text{NR}}a_0 + iGb_0, \quad (\text{S28})$$

Here,  $s_{\text{in}} = \sqrt{P_{\text{in}}/\hbar\omega_0}$ , and  $|s_{\text{in}}|^2$  represents the photon flux of the pump. At the steady state, the intracavity field yields

$$b_0 = \frac{\sqrt{\kappa_{e,\text{RC}}}}{i\left(\delta\omega_{\text{RC}} - \frac{G^2\delta\omega_{\text{NR}}}{\delta\omega_{\text{NR}}^2 + \kappa_{\text{NR}}^2/4}\right) + \frac{\kappa_{\text{RC}}}{2} + \frac{G^2\kappa_{\text{NR}}/2}{\delta\omega_{\text{NR}}^2 + \kappa_{\text{NR}}^2/4}} \cdot s_{\text{in}}, \quad (\text{S29})$$

$$a_0 = \frac{iG\sqrt{\kappa_{e,\text{RC}}}}{i\left(\frac{\delta\omega_{\text{RC}}\kappa_{\text{NR}} + \delta\omega_{\text{NR}}\kappa_{\text{RC}}}{2}\right) - \delta\omega_{\text{RC}}\delta\omega_{\text{NR}} + \frac{\kappa_{\text{RC}}\kappa_{\text{NR}}}{4} + G^2} \cdot s_{\text{in}}. \quad (\text{S30})$$

According to the input-output formalism,

$$s_{\text{out,RC}} = -s_{\text{in}} + \sqrt{\kappa_{e,\text{RC}}}b_0, \quad (\text{S31})$$



$$s_{\text{out,NR}} = \sqrt{\kappa_{e,\text{NR}}} a_0, \quad (\text{S32})$$

where  $s_{\text{out,RC(NR)}}$  represents the output field at the through (drop) port. Thus, the transmission spectra at the through and drop are expressed as

$$\left| \frac{s_{\text{out,RC}}}{s_{\text{in}}} \right|^2 = \frac{\left( \delta\omega_{\text{RC}} - \frac{G^2 \delta\omega_{\text{NR}}}{\delta\omega_{\text{NR}}^2 + \kappa_{\text{NR}}^2/4} \right)^2 + \left( \frac{\kappa_{0,\text{RC}} - \kappa_{e,\text{RC}}}{2} + \frac{G^2 \kappa_{\text{NR}}/2}{\delta\omega_{\text{NR}}^2 + \kappa_{\text{NR}}^2/4} \right)^2}{\left( \delta\omega_{\text{RC}} - \frac{G^2 \delta\omega_{\text{NR}}}{\delta\omega_{\text{NR}}^2 + \kappa_{\text{NR}}^2/4} \right)^2 + \left( \frac{\kappa_{\text{RC}}}{2} + \frac{G^2 \kappa_{\text{NR}}/2}{\delta\omega_{\text{NR}}^2 + \kappa_{\text{NR}}^2/4} \right)^2}, \quad (\text{S33})$$

$$\left| \frac{s_{\text{out,NR}}}{s_{\text{in}}} \right|^2 = \frac{G^2 \kappa_{e,\text{RC}} \kappa_{e,\text{NR}}}{\left( \frac{\delta\omega_{\text{RC}} \kappa_{\text{NR}} + \delta\omega_{\text{NR}} \kappa_{\text{RC}}}{2} \right)^2 + \left( \delta\omega_{\text{RC}} \delta\omega_{\text{NR}} - \frac{\kappa_{\text{RC}} \kappa_{\text{NR}}}{4} - G^2 \right)^2}. \quad (\text{S34})$$

Based on the above equations, the calculated resonant frequencies of RC and NR relative to the pump for the three stages presented in Fig. 3C are:  $\delta\omega_{\text{NR}}/2\pi = 0.34$  GHz,  $\delta\omega_{\text{RC}}/2\pi = 3.27$  GHz for soliton initializing,  $\delta\omega_{\text{NR}}/2\pi = 1.24$  GHz,  $\delta\omega_{\text{RC}}/2\pi = 1.24$  GHz for swapping, and  $\delta\omega_{\text{NR}}/2\pi = 8.9$  GHz,  $\delta\omega_{\text{RC}}/2\pi = 0.3$  GHz for soliton broadening.

### III. ADDITIONAL CHARACTERIZATION OF MICROCOMBS

#### A. Optical spectrum

Figure S7 shows the optical spectra recorded at both the drop and through ports while NR is operating in the ultrabroad soliton microcomb state, under a pump power of 290 mW applied to the bus waveguide. Notably, the spectrum obtained from the through port exhibits high-power comb lines, which is attributed to mode crossings induced by the vernier effect between the resonances of NR and RC<sup>7</sup> (fig. S4A).

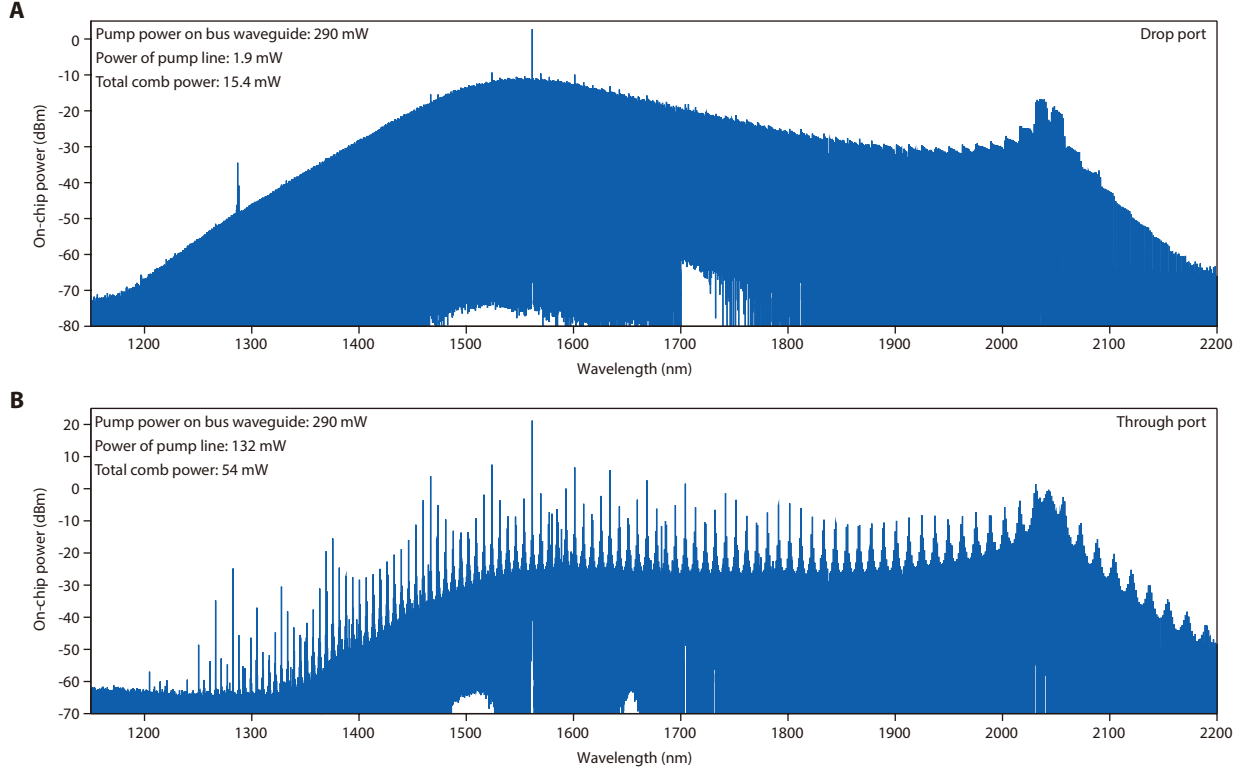


**Fig. S7. Optical spectra of the ultra-broadband soliton microcomb.** (A) Spectrum from the drop port. (B) Spectrum from the through port.

## B. Autocorrelation

The temporal profile of the soliton microcomb is characterized using an autocorrelator (APE pulseCheck), where the dispersion is compensated using a dispersion-compensating fiber. Fitting of the autocorrelation trace reveals that the soliton pulse exhibits a full-width-at-half-maximum (FWHM) of 42.7 fs (fig. S8). It should be noted that the measured FWHM exceeds the 15.84 fs FWHM inferred from the optical spectrum (fig. S7), likely due to the limited bandwidth offered by the frequency-doubling crystal in the autocorrelator.

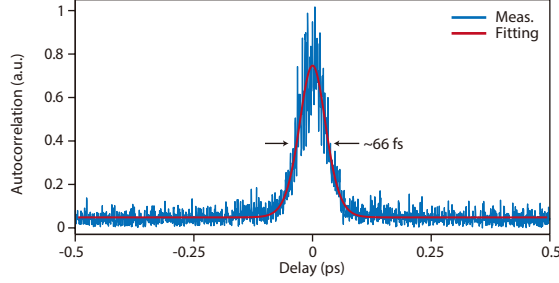


**Fig. S8. Intensity autocorrelation of the ultra-broadband soliton microcomb.** The full-width-at-half-maximum of the autocorrelation trace is 66 fs.

## C. Coherence

The repetition rate of the soliton microcomb is determined via electro-optic (EO) downconversion<sup>8</sup> (fig. S9A). In this measurement, two adjacent comb lines are isolated using a band-pass filter and subsequently modulated with a phase modulator operating at  $f_{\text{RF}} = 40$  GHz. This modulation generates sidebands around each comb line, and a pair of sidebands are selected by an additional band-pass filter. The resulting low-frequency beat note,  $f_{\text{beat}}$ , is detected by a high-speed photodetector. By measuring the beat note using an electrical spectral analyzer, we can deduce the comb spacing, which is given by

$$f_{\text{rep}} = 2f_{\text{RF}} + f_{\text{beat}}. \quad (\text{S35})$$

In our experiments,  $f_{\text{beat}} = 16.888$  GHz, yielding a soliton microcomb repetition rate of  $f_{\text{rep}} = 96.888$  GHz. The phase noise of the downconverted beat note,  $S_{\phi, \text{beat}}$ , is related to the phase noise of the repetition rate,  $S_{\phi, \text{rep}}$ , and that of the RF source,  $S_{\phi, \text{RF}}$ , according to

$$S_{\phi, \text{beat}} = S_{\phi, \text{rep}} + 4S_{\phi, \text{RF}}. \quad (\text{S36})$$

Figure S9B presents the measured phase noise of the downconverted beatnote using a phase noise analyzer. For offset frequencies below 10 kHz,  $S_{\phi, \text{beat}}$  predominantly reflects  $S_{\phi, \text{rep}}$ , as  $S_{\phi, \text{RF}}$  is comparatively negligible. At offset frequencies above 30 kHz, the noise is primarily limited by the RF source. These findings demonstrate the mutual coherence of the generated ultra-broadband soliton microcomb.

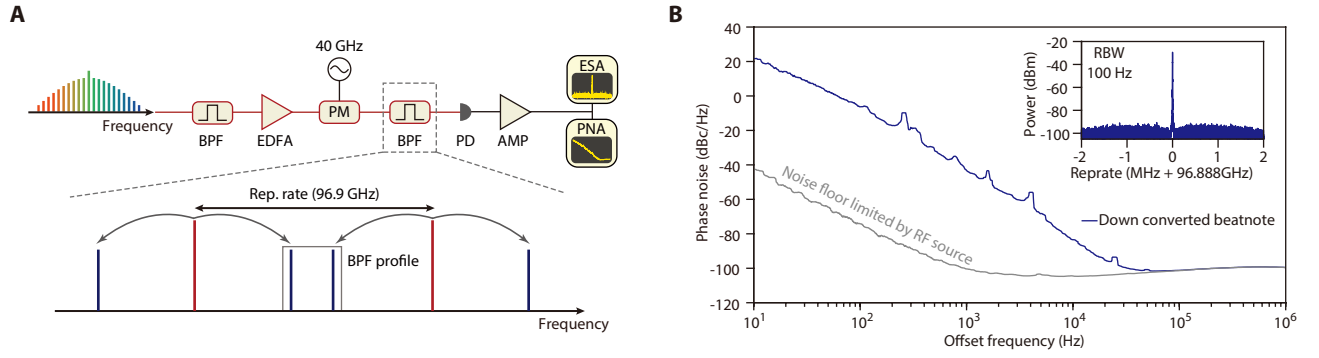


**Fig. S9. Coherence of the ultra-broadband soliton microcomb.** (A) Experimental setup for electro-optic (EO) down-conversion. BPF: band-pass filter; EDFA: erbium-doped fiber amplifier; PM: phase modulator; PC: polarization controller; PD: photodetector; AMP: electrical amplifier; ESA: electrical spectral analyzer; PNA: phase noise analyzer. The lower schematic illustrates the phase-modulated microcomb spectra entering the BPF, where adjacent microcomb modes (red) and EO-modulated sidebands (blue) overlap to produce the downconverted beat note. (B) Single-sideband phase noise of the downconverted beat note, along with the RF source contribution. Inset: beat note corresponding to the microcomb repetition frequency. RBW: resolution bandwidth.

- 
- [1] Bao, C. *et al.* Nonlinear conversion efficiency in kerr frequency comb generation. *Opt. Lett.* **39**, 6126–6129 (2014).
  - [2] Herr, T. *et al.* Temporal solitons in optical microresonators. *Nat. Photon* **8**, 145–152 (2014).
  - [3] Godey, C., Balakireva, I. V., Coillet, A. & Chembo, Y. K. Stability analysis of the spatiotemporal lugiato-lefever model for kerr optical frequency combs in the anomalous and normal dispersion regimes. *Phys. Rev. A* **89**, 063814 (2014).
  - [4] Parra-Rivas, P., Gomila, D., Matías, M. A., Coen, S. & Gelens, L. Dynamics of localized and patterned structures in the lugiato-lefever equation determine the stability and shape of optical frequency combs. *Phys. Rev. A* **89**, 043813 (2014).
  - [5] Wang, Y. *et al.* Compact turnkey soliton microcombs at microwave rates via wafer-scale fabrication. *arXiv preprint arXiv:2502.10941* (2025).
  - [6] Luo, Y.-H. *et al.* A wideband, high-resolution vector spectrum analyzer for integrated photonics. *Light Sci. Appl.* **13**, 83 (2024).
  - [7] Hu, Y. *et al.* High-efficiency and broadband on-chip electro-optic frequency comb generators. *Nat. Photon.* **16**, 679–685 (2022).
  - [8] Del’Haye, P., Papp, S. B. & Diddams, S. A. Hybrid electro-optically modulated microcombs. *Phys. Rev. Lett.* **109**, 263901 (2012).